In Phantom Validation of Time-Domain Near-Infrared Optical Tomography Pioneer for Imaging Brain Hypoxia and Hemorrhage

Jiang, J.; Lindner, S.; Di Costanzo-Mata, A.; Zhang, C.; Charbon, E.; Wolf, M.; Kalyanov, A.

DOI
10.1007/978-3-030-48238-1_54

Publication date
2021

Document Version
Final published version

Published in
Oxygen transport to Tissue XLII

54

In Phantom Validation of Time-Domain Near-Infrared Optical Tomography Pioneer for Imaging Brain Hypoxia and Hemorrhage

J. Jiang, S. Lindner, A. Di Costanzo-Mata, C. Zhang, E. Charbon, M. Wolf, and A. Kalyanov

Abstract

The neonatal brain is a vulnerable organ, and lesions due to hemorrhage and/or ischemia occur frequently in preterm neonates. Even though neuroprotective therapies exist, there is no tool available to detect the ischemic lesions. To address this problem, we have recently designed and built the new time-domain near-infrared optical tomography (TD NIROT) system – Pioneer. Here we present the results of a phantom study of the system performance. We used silicone phantoms to mimic risky situations for brain lesions: hemorrhage and hypoxia. Employing Pioneer, we were able to reconstruct accurately both position and optical properties of these inhomogeneities.

Keywords

Time-domain near-infrared optical tomography (TD NITOR) · Diffuse optical tomography · Tissue optical properties reconstruction · Tissue oxygenation · Preterm brain imaging

J. Jiang · A. Di Costanzo-Mata · M. Wolf
A. Kalyanov (✉)
Biomedical Optics Research Laboratory (BORL), Department of Neonatology, University of Zurich and University Hospital Zurich, Zurich, Switzerland
e-mail: alexander.kalyanov@usz.ch

S. Lindner
Biomedical Optics Research Laboratory (BORL), Department of Neonatology, University of Zurich and University Hospital Zurich, Zurich, Switzerland

Advanced Quantum Architecture (AQUA) laboratory, School of Engineering, EPFL Lausanne, Lausanne, Switzerland

C. Zhang
Applied Quantum Architectures, Delft University of Technology, Delft, the Netherlands

E. Charbon
Advanced Quantum Architecture (AQUA) laboratory, School of Engineering, EPFL Lausanne, Lausanne, Switzerland

Applied Quantum Architectures, Delft University of Technology, Delft, the Netherlands

54.1 Introduction

The brain of extreme preterms is subject to injuries due to the too low or too high oxygenation in the brain tissue. Both hemorrhage and ischemia occur frequently in preterm neonates. Happening early in life, they often lead to long-term disabilities. Despite an improved survival rate (~80%), up to 25% of extremely preterm infants develop cerebral palsy or a low IQ, and a significant cognitive delay is present in ~12% by school age [1, 2]. Neuroprotective therapies exist and are available to clinicians. However, there is no tool that can detect ischemia or hypoxia at the bedside. Cranial ultrasound (cUS) is frequently applied in

E. M. Nemoto et al. (eds.), *Oxygen Transport to Tissue XLII*, Advances in Experimental Medicine and Biology 1269, https://doi.org/10.1007/978-3-030-48238-1_54

neonatology, because the fontanel provides a window to the brain. Although cUS provides anatomical images of the brain and cerebral blood flow velocity (CBFV), it is insensitive to hypoxia (low tissue oxygen saturation (StO_2)). A lesion can be identified only once the tissue degraded. MRI measures cerebral blood flow (CBF), e.g., by arterial spin labeling, but StO_2 cannot be determined, and the method is rarely applied in intensive care [3, 4], because it is not bedside, and requires a risky transport of the vulnerable patient.

The most promising noninvasive method so far is near-infrared spectroscopy (NIRS) [5–8], which measures the StO_2, which reflects the proportion of hemoglobin carrying oxygen in the field of view of NIRS. Even though NIRS provides StO_2 values of brain tissue, the technology lacks spatial resolution. Thus, it cannot provide a full picture of cerebral StO_2, since the hypoxia of brain is a localized event [9].

Another approach is time-domain near-infrared optical tomography (TD NIROT) which provides 3D images of StO_2. In TD NIROT, a set of light sources and detectors is arranged over the tissue. Light intensity and photon time-of-flight (ToF) between emission and detection are measured for each source-detector pair [10, 11]. The measured data is then fed into an image reconstruction method based on a physical model for light propagation in tissue. It has been shown that, using short source detector distances and photons with "long" TOFs, TD NIROT is able to reach a depth of 60 mm [12].

State-of-the-art NIROT technology is currently based on photomultiplier tubes [13]. Due to the bulkiness of such systems, the number of detectors that can be used in a system is limited to a few dozen [13, 14], and it would be impossible to increase this number by a factor of 10. The next generation of detectors – single-photon avalanche photodiodes (SPADs) – enables a significant increase in the number of detectors, which leads to better spatial resolution [15–17].

To benefit from this new technology, we have recently designed and built the new TD NIROT system – Pioneer [18]. It aims at imaging the brain of preterm neonates with a high spatial resolution and at detecting hypoxia and bleeding. Here the aim was to study the system performance in a silicone phantom that mimics risky situations for brain lesions: hemorrhage and hypoxia. These are characterized by different optical properties and location.

54.2 Methods

Pioneer is a TD NIROT system based on a time-of-flight camera with 1024 pixels (Fig. 54.1). Each pixel comprises a SPAD with 116 ps time resolution and an unprecedented sensitivity of 12% at 800 nm. This camera chip was specifically designed for NIROT by Biomedical Optics Research Laboratory, University of Zurich and University Hospital Zurich, Switzerland (BORL) and Advanced Quantum Architecture laboratory, School of Engineering, EPFL Lausanne, Switzerland (AQUA) [19]. Pioneer is equipped with a super continuum laser (SuperK Extreme-15, NKT, Denmark) connected through optical fibers to 11 light sources arranged in a circle around the field of view (FoV) (Fig. 54.1). Altogether, we employed almost 4000 source-detector pairs. Emission wavelength can be set in a wide NIR range (650–950 nm); consequently, the system enables multispectral tomography of tissue. Thus, detection of multiple chromophores, such as oxy- and deoxyhemoglobin, fat, water, etc., is possible. Three wavelengths were employed in this work: 689 nm, 802 nm, and 838 nm. For more details on Pioneer, consult our previous publications [18, 20, 21].

We created a silicone phantom with an inclusion to test the system. The phantom has a cylindrical shape: Ø110 × 62 mm^3. It is large enough to ensure the absence of influence from boundaries on the light propagation. The inclusion, a Ø10 × 30 mm^3 cylinder, was located at 15 mm depth at the center of the phantom (Fig. 54.2a). This phantom was manufactured in two steps: (i) the inclusion of desired shape was made out of silicone with certain inks added to achieve the optical properties [22]; (ii) after curing, the inclusion was placed in the mold for the phantom and fixed at the chosen location by fishing rope; then the mold was filled with silicone with bulk optical properties.

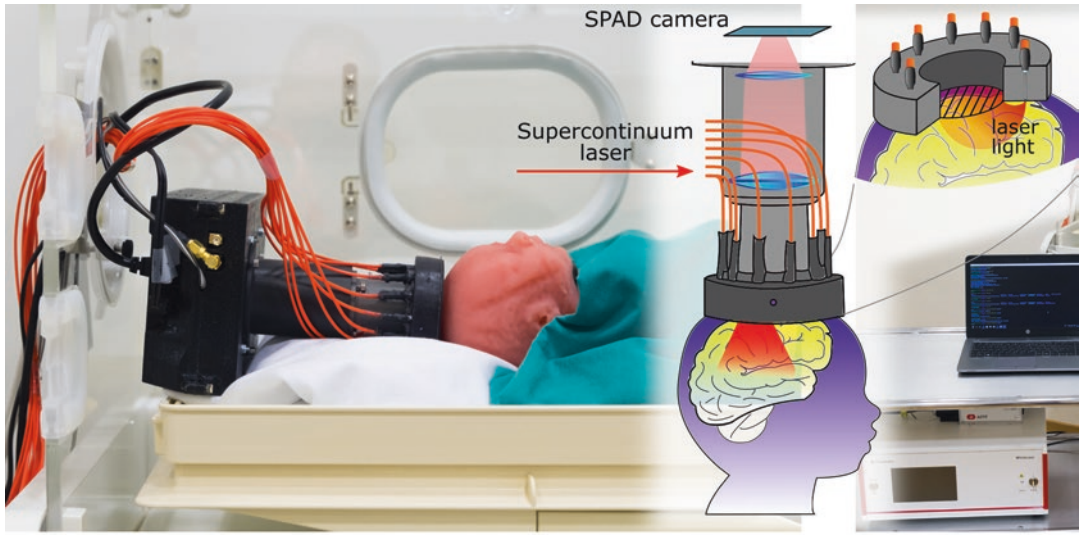

Fig. 54.1 Pioneer tomography setup. The image shows schematic of Pioneer probe design (center), the actual sensor placed inside neonatology intensive care unit (NICU) and applied to dummy baby head (left), and the overview of the whole system including bulky components placed next to the NICU (right)

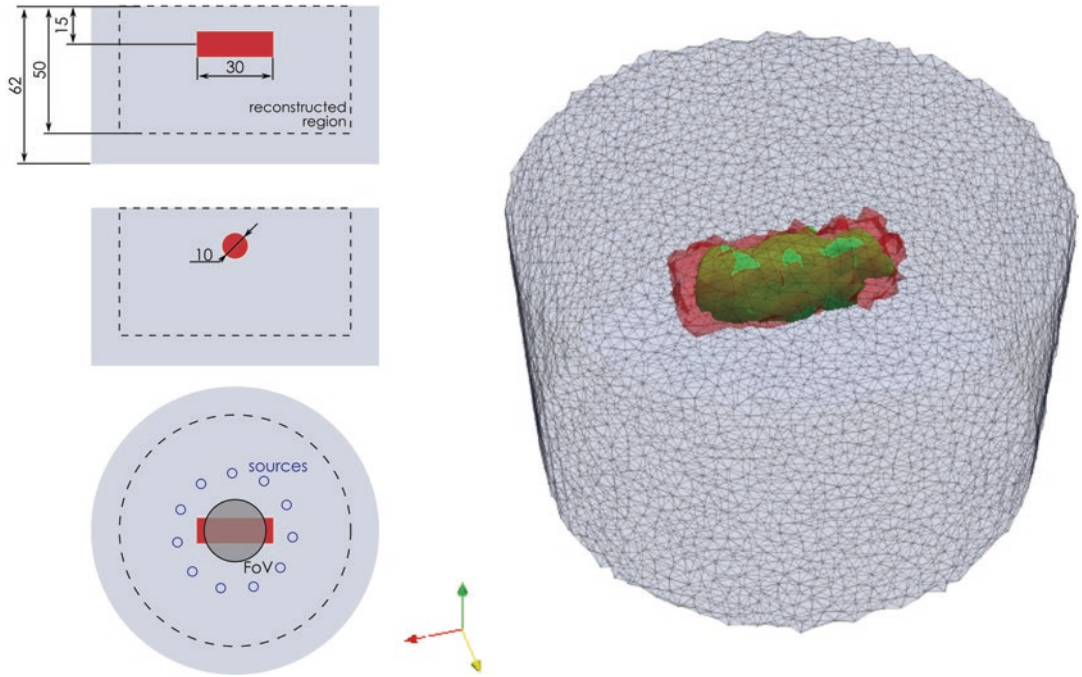

Fig. 54.2 Schematic of silicone phantom with inclusion (left) and reconstructed 3D image (center and right): ground truth in red, reconstructed inhomogeneity in green

Once cured, we removed fishing rope from the phantom. Due to its flexibility and elasticity, the silicone expanded into the cavities and completely closed them.

Optical properties of the bulk and the inclusion were measured with frequency domain NIRS Imagent (ISS; USA) [23]. We give these values in Table 54.1. Absorption of the bulk was

Table 54.1 Optical properties of the phantom and the MC reconstructed values

λ	Inclusion	Contrast	μ_s' [cm^{-1}]	μ_a bulk [cm^{-1}]			μ_a of inclusion [cm^{-1}]		
[nm]	Type		Bulk/inclusion	Target[b]	Meas	Diff	Target[b]	Meas	Diff
689	Hemorrhage	7×	8.1/9.5	0.055	0.050	**−10%**	[a]0.366	0.320	**−14%**
802	–	3×	6.9/8.3	0.055	0.054	**−2%**	0.187	0.187	**0%**
838	Hypoxia	2×	6.7/8.0	0.055	0.069	**21%**	0.124	0.162	**24%**

μ_s' reduced scattering coefficient, μ_a absorption coefficient
[a]Measured with ±15% accuracy due to high μ_a
[b]±10% error

constant at the wavelengths of interest, whereas absorption of the inclusion was wavelength dependent. It enabled us to achieve various contrasts between the inclusion and the surrounding media (see Table 54.1). Namely, the contrast varied from 2× (hypoxia) to 7× (hemorrhage) depending on the wavelength. This high contrast is typical for hemorrhage lesion due to the high concentration of hemoglobin. Despite the wavelength-dependent absorption spectra of the inclusion, we did not aim at modeling an actual spectrum of tissue but rather created a model for several distinct cases of lesion. We also produced a homogeneous phantom with the same bulk optical properties and used it as a reference in the reconstruction, i.e., scaled simulated signal by the one measured on the homogeneous phantom to correct for artifacts related to hardware (e.g., intensity and time offset related to different sources). Alternatively, wavelength normalization method can be used instead, as it was recently reported [26, 27]. However, we did not employ the method in this work.

We performed two types of reconstructions. First, we reconstructed spatial distribution of absorption coefficient within the phantom based on 689 nm data. We chose this wavelength due to the highest contrast. This reconstruction was performed in the NIRFAST package for Matlab (finite element method FEM) [24]. Next, we segmented the model based on this reconstruction. All nodes with absorption below a certain threshold were assigned to segment 1 (bulk), whereas nodes above the threshold were assigned to segment 2 (inclusion). The threshold was set as 50% difference between maximum and minimum reconstructed absorption. Finally, we performed a hard prior reconstruction on the segmented mesh at all three wavelengths based on MCX (Monte Carlo MC) [25][28].

54.3 Results and Discussion

54.3.1 No-Prior Reconstruction

Reconstruction of an inclusion position without prior information is not trivial, since the problem is ill posed. Nevertheless, Pioneer provides a rich set of data, which enable us to reconstruct the inclusion inside the phantom.

The reconstructed inhomogeneity agrees with the inclusion in both shape and location (Fig. 54.2). However, we noticed a mismatch on both sides of the cylinder due to its length exceeding the field-of-view (FoV) of Pioneer (Fig. 54.2a). Please note that we reduced the reconstructed region as compared to the real phantom IN order to achieve faster reconstruction. This is not expected to affect the reconstruction quality since the reconstructed region is large enough to avoid the influence from boundaries.

The no-prior reconstruction was run on the data acquired at 689 nm. At this wavelength, the phantom has 6.7× contrast between bulk and inclusion absorption coefficients. This contrast is well within physiological values. A hemorrhage, i.e., a volume with a high hemoglobin concentration, has a contrast of a factor 50 compared to the bulk tissue.

54.3.2 Region-Based Reconstruction

In a region-based reconstruction, the problem is simplified by implementing a known geometry and structure of the object. Such information can be employed by the no-priors reconstruction. An area with similar optical properties is treated as a single region. Therefore, the number of unknowns is limited by the number of regions. In our case, we had only two regions (bulk and inclusion).

We performed a MC reconstruction of absorption for three wavelengths: 689, 802, and 838 nm. The results are presented in Table 54.1. We achieved good agreement for shorter wavelengths at which the contrast between the inclusion and the bulk was high: 6.7× at 689 nm and 3.4× at 802 nm. At 838 nm, the contrast was only 2.3×. Here we observed an offset. It has to be considered that the true values were measured with an error of ±10%.

As expected, a priori structural information enabled accurate reconstruction of optical properties. The low contrast case, which imitated hypoxia, demonstrated an increased relative error (Table 54.1), whereas, the error was ≤10% for the high contrast cases, which is similar to a hemorrhage.

54.4 Conclusions

The new high-resolution time-domain near-infrared optical tomography system Pioneer was built and tested on a silicone phantom. We were able to achieve good agreement in the geometry and optical properties between the reconstructed image and the ground truth. Thus, an important step in the translation of Pioneer to detect ischemia and hemorrhage in the brain of preterms was mastered.

Acknowledgments This research was supported by Swiss Cancer Research grant KFS-3732-08-2015, the Swiss National Science Foundation project 159490, the National Competence Center in Biomedical Imaging (NCCBI), and CONACyT by the CVU-627802. MW declares that he is founder and president of the board of OxyPrem AG.

References

1. Fischer N, Steurer MA, Adams M et al (2009) Survival rates of extremely preterm infants (gestational age <26 weeks) in Switzerland: impact of the Swiss guidelines for the care of infants born at the limit of viability. Arch Dis Child Fetal Neonatal Ed 94:F407–F413
2. Hutchinson EA, De Luca CR, Doyle LW et al (2013) School-age outcomes of extremely preterm or extremely low birth weight children. Pediatrics 131:e1053–e1061
3. Tortora D, Mattei PA, Navarra R et al (2017) Prematurity and brain perfusion: arterial spin labeling MRI. Neuroimage Clin 15:401–407
4. De Vis JB, Hendrikse J, Petersen ET et al (2015) Arterial spin-labelling perfusion MRI and outcome in neonates with hypoxic-ischemic encephalopathy. Eur Radiol 25:113–121
5. Scholkmann F, Kleiser S, Metz AJ et al (2014) A review on continuous wave functional near-infrared spectroscopy and imaging instrumentation and methodology. Neuroimage 1:6–27
6. Hyttel-Sorensen S, Pellicer A, Alderliesten T et al (2015) Cerebral near infrared spectroscopy oximetry in extremely preterm infants: phase II randomised clinical trial. BMJ 350:g7635
7. Alderliesten T, van Bel F, van der Aa NE et al (2018) Low cerebral oxygenation in preterm infants is associated with adverse neurodevelopmental outcome. J Pediatr 207:109–116
8. van Bel F, Mintzer JP (2018) Monitoring cerebral oxygenation of the immature brain: a neuroprotective strategy? Pediatr Res 84:159–164
9. Guo T, Duerden EG, Adams E et al (2017) Quantitative assessment of white matter injury in preterm neonates. Association with outcomes. Neurology 88:614–622
10. Zhao H, Gao F, Tanikawa Y et al (2007) Time-resolved diffuse optical tomography and its application to in vitro and in vivo imaging. J Biomed Opt 12:062107
11. Gibson AP, Hebden JC, Arridge SR (2005) Recent advances in diffuse optical imaging. Phys Med Biol 50:R1–R43
12. Pifferi A, Contini D, Mora AD et al (2016) New frontiers in time-domain diffuse optics, a review. J Biomed Opt 21:091310
13. Yamada Y, Suzuki H, Yamashita Y (2019) Time-domain near-infrared spectroscopy and imaging: a review. Appl Sci 9(6):1127
14. Hebden JC, Austin T (2007) Optical tomography of the neonatal brain. Eur Radiol 17:2926–2933
15. Dalla Mora A, Contini D, Arridge S et al (2015) Towards next-generation time-domain diffuse optics for extreme depth penetration and sensitivity. Biomed Opt Express 6:1749–1760
16. Villa F, Lussana R, Bronzi D et al (2014) CMOS imager with 1024 SPADs and TDCs for single-photon timing and 3-D time-of-flight. IEEE J Sel Top Quant 20(6):364–373
17. Sawosz PL, Kacprzak M, Zolek NS et al (2010) Optical system based on time-gated, intensified charge-coupled device camera for brain imaging studies. J Biomed Opt 15:1–7, 7
18. Kalyanov A, Jiang J, Lindner S, et al (2018) Time domain near-infrared optical tomography with time-of-flight spad camera: the new generation. Optical Society of America, City, p OF4D.5
19. Lindner S, Zhang C, Antolovic IM, et al (2018) A novel 32 × 32, 224 mevents/s time resolved SPAD image sensor for near-infrared optical tomography. Optical Society of America, City, p JTh5A.6

20. Kalyanov A, Jiang J, Lindner S, et al (2018) TR NIROT system 'Pioneer' for preterm brain imaging: in-phantom tests, City
21. Di Costanzo Mata A, Jiang H, Lindner S, et al (2018) Time-resolved NIROT Pioneer system for imaging of human tissue and preterm-infant brain oxygenation, City
22. Tomm N, Ahnen L, Isler H et al (2018) Characterization of the optical properties of color pastes for the design of optical phantoms mimicking biological tissue. J Biophotonics 12(4):e201800300
23. Hueber DM, Fantini S, Cerussi AE, et al (1999) New optical probe designs for absolute (self-calibrating) NIR tissue hemoglobin measurements. SPIE
24. Dehghani H, Srinivasan S, Pogue BW et al (2009) Numerical modelling and image reconstruction in diffuse optical tomography. Philos Transact A Math Phys Eng Sci 367:3073–3093
25. Fang Q, Boas DA (2009) Monte Carlo simulation of photon migration in 3D turbid media accelerated by graphics processing units. Opt Express 17:20178–20190
26. Stanislaw Wojtkiewicz, Anna Gerega, Marta Zanoletti, Aleh Sudakou, Davide Contini, Adam Liebert, Turgut Durduran, Hamid Dehghani, (2019) Self-calibrating time-resolved near infrared spectroscopy. Biomedical Optics Express 10 (5):2657
27. Jingjing Jiang, Aldo Di Costanzo Mata, Scott Lindner, Chao Zhang, Edoardo Charbon, Martin Wolf, Alexander Kalyanov, (2020) Image reconstruction for novel time domain near infrared optical tomography: towards clinical applications. Biomedical Optics Express 11 (8):4723
28. Jingjing Jiang, Martin Wolf, Salvador Sánchez Majos, (2016) Fast reconstruction of optical properties for complex segmentations in near infrared imaging. Journal of Modern Optics 64 (7):732–742